# m-NLP inference models using simulation and regression techniques

**Guangdong Liu[1], Sigvald Marholm [2,3], Anders J. Eklund[4], Lasse Clausen[2], Richard Marchand[1]**

[1]Department of Physics, University of Alberta, Edmonton, AB, Canada
[2]Department of Physics, University of Oslo, Oslo, Norway
[3]Department of Computational Materials Processing, Institute for Energy Technology, Kjeller, Norway
[4]Materials Physics Oslo, SINTEF Industry, Oslo, Norway

**Key Points:**

- Multivariate regression models are constructed and assessed using synthetic data sets created from kinetic simulations for m-NLP inferences.
- Trained models are applied to in situ measurements reported for fixed bias multi-Needle Langmuir Probes (m-NLP) on NorSat-1 satellite.
- Consistency checks are made to further demonstrate the applicability of model inferences to satellite measurements.

Corresponding author: Guangdong Liu, guangdon@ualberta.ca

## Abstract

Current inference techniques for processing multi-needle Langmuir Probe (m-NLP) data are often based on the Orbital Motion-Limited (OML) theory which relies on several simplifying assumptions. Some of these assumptions, however, are typically not well satisfied in actual experimental conditions, thus leading to uncontrolled uncertainties in inferred plasma parameters. In order to remedy this difficulty, three-dimensional kinetic particle in cell simulations are used to construct synthetic data sets, which are then used to train and validate regression-based models capable of inferring electron density and satellite potentials from 4-tuples of currents collected with fixed-bias needle probes similar to those on the NorSat-1 satellite. Based on our synthetic data, the techniques presented enable excellent inferences of the plasma density, and floating potentials, while the generally accepted OML inferred densities are approximately three times too high. The new inference techniques that we propose, are applied to NorSat-1 data, and compared with OML inferences. While both regression and OML based inferences of floating potentials agree well with synthetic data, only regression inferred potentials are consistent with satellite measured currents, indicating that the regression based inference models are more robust and accurate when applied to satellite data.


## 1 Introduction

Langmuir probes are widely used to characterize space plasma and laboratory plasma. A variety of Langmuir probe geometries are being used, such as spherical (Bhattarai & Mishra, 2017), cylindrical (Hoang, Clausen, et al., 2018), and planar probes (Lira et al., 2019; Johnson & Holmes, 1990; Sheridan, 2010). Probes can be operated in sweep mode (Lebreton et al., 2006), harmonic mode (Rudakov et al., 2001), or fixed biased mode (Jacobsen et al., 2010), for different types of missions and measurements. Despite differences, all Langmuir probes consist of conductors exposed to plasma to collect current as a function of bias voltage. A common approach to infer plasma parameters from Langmuir probes is to sweep the bias voltage and produce a current-voltage characteristic, which can be analyzed using theories such as the Orbital Motion-Limited (OML) (Mott-Smith & Langmuir, 1926) theory, the Allen-Boyd-Reynolds (ABR) theory (Allen et al., 1957; Chen, 1965, 2003), and the Bernstein-Rabinowitz-Laframboise (BRL) theory (Bernstein & Rabinowitz, 1959; Laframboise, 1966) to obtain plasma parameters such as density, temperature, and satellite floating potential. The temporal and, on a satellite, the spatial resolution of Langmuir probe measurements is determined by the sweep time, which is typically on the order of 1 s (Jacobsen et al., 2010). Considering the orbital speed to be around 7500 m/s for a typical satellite in low Earth orbit (LEO), this sampling rate imposes a lower bound on the spatial resolution of measurements, which cannot be lower than $\sim 10$ km. In order to overcome this problem, Jacobsen suggested the use of multiple fixed biased needle probes (m-NLPs) to sample plasma simultaneously at different bias potentials in the electron saturation region (Jacobsen et al., 2010). This approach eliminates the need for sweeping the bias voltage, and greatly increases the sampling rate of the instrument.

Previous inference models for m-NLPs rely on the OML approximation, from which the current $I_e$ collected by a needle probe in the electron saturation region is approximated as:

$$I_e = -n_e e A \frac{2}{\sqrt{\pi}} \sqrt{\frac{kT_e}{2\pi m_e}} \left(1 + \frac{e(V_f + V_b)}{kT_e}\right)^{\beta}, \tag{1}$$

where $n_e$ is the electron density, $A$ is the probe surface area, $e$ is the elementary charge, $k$ is Boltzmann's constant, $T_e$ is the electron temperature, $V_f$ is the satellite floating potential, $V_b$ is the bias potential of the probe with respect to the satellite, and $\beta$ is a parameter related to probe geometry, density, and temperature (Marholm & Marchand, 2020; Hoang, Røed, et al., 2018). Several assumptions were made in the derivation of this inference equation; a key one being that the probe length is much larger than the Debye length. If this assumption is valid, then $\beta = 0.5$, and as first suggested by Jacobsen, a set of m-NLPs can be used to infer the density independently of the temperature (Jacobsen et al., 2010). For a satellite in near-Earth orbit at altitudes ranging from 450 km to 600 km, we can expect a Debye length of around 2-50 mm. A common length for m-NLP instrument used on small satellites is $\sim 25$ mm (Bekkeng et al., 2010; Hoang, Clausen, et al., 2018; Hoang et al., 2019), which is often comparable to, and sometimes smaller than the Debye length. One consequence is that the $\beta = 0.5$ assumption does not hold, and Eq. 1 is a better approximation with a $\beta$ value between 0.5 and 1. For example, in a hot filament-generated plasma experiment, Sudit and Woods showed that $\beta$ can reach 0.75 for a ratio between the Debye length and the probe length in the range of 1 to 3. For larger Debye lengths, they also observed an expansion of the probe sheath from a cylindrical shape into a spherical shape (Sudit & Woods, 1994). In the ICI-2 sounding rocket experiment, $\beta$ calculated from three 25 mm m-NLPs varied between 0.3 to 0.7 in an altitude ranging from 150 to 300 km(Hoang, Røed, et al., 2018). Simulation results by Marholm et al. showed that even a 50 mm probe can be characterized by a $\beta \sim 0.8$ (Marholm et al., 2019), in disagreement with the OML theory. In practice, needle probes are mounted on an electrically isolated and equipotential guard in order to attenuate end effects on the side to which it is attached. The distribution of the current collected per unit length is nonetheless not uniform along the probe, as more current is collected near the end opposite to the guard. A study by Marholm & Marchand showed that for a cylindrical probe length that is 10 times the Debye length, $\beta$ is approximately 0.72. For a probe length that is 30 times the Debye length, $\beta$ is approximately 0.62, and with a guard, this number is reduced to 0.58 (Marholm & Marchand, 2020). Although this number approaches 0.5, 30 times the Debye length is a stringent requirement for OML to be valid, and it is hardly ever fulfilled in practice. Experimentally, Hoskinson and Hershkowitz showed that even with a probe length 50 times the Debye length, $\beta$ is approximately 0.6, and the density inference based on an ideal $\beta = 0.5$ is 25 % too high (Hoskinson & Hershkowitz, 2006). Barjatya estimated that even a 10% error in $\beta$ (to 0.55) can result in a 30 % or more relative error in the calculated density based on the $\beta = 0.5$ assumption (Barjatya & Merritt, 2018). In this study, densities estimated using Eq. 1 are about three times larger than the known values used as input in our simulations, as illustrated in section 3.1.

In the following, we present and assess new techniques to infer plasma densities, and satellite potentials from fixed bias needle probe measurements while accounting for finite length effects of the probes. Our approach, described in Sec. 2, makes use of kinetic simulations to construct synthetic data sets, consisting of calculated currents and known densities, temperatures, and satellite potentials used as input in the simulations. In Sec. 3 regression models are constructed and assessed by applying them to synthetic data. The models trained with synthetic data are then applied to NorSat-1 data in Sec. 4 by inferring densities and satellite floating potentials from in situ measured currents. Section 5 summarizes our findings and presents some concluding remarks.

## 2 Methodology

In this section, we briefly describe our kinetic simulation approach, and how it is used to construct synthetic data sets used to train and validate inference models, using two regression techniques.

### 2.1 Kinetic simulations

The plasma conditions considered in this study are selected to be relevant to plasma conditions that a spacecraft could encounter in a low Earth orbit at altitudes ranging between 550 and 650 km. This is done by sampling plasma parameters using the International Reference Ionosphere (IRI) (Bilitza et al., 2014) model at different latitudes,

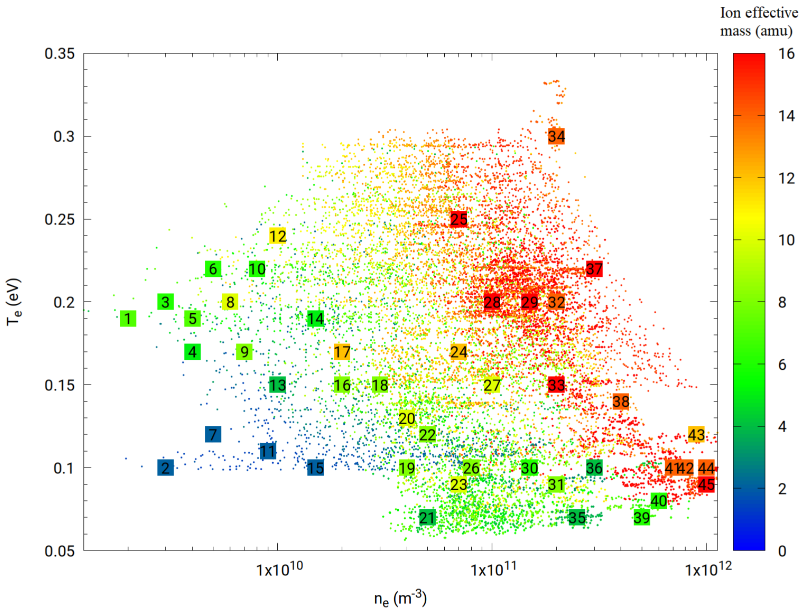


**Figure 1.** Scatter plot of plasma parameters obtained from the IRI model, corresponding to different latitudes, longitudes, altitudes, and times, as listed in Table 1. The x and y axes, and the color bar refer respectively, to the electron density and temperature, and the ion effective mass. Numbered squares identify the set of parameters used in the kinetic simulations.

longitudes, altitudes, and times as shown in Fig. 1. The ranges considered for these parameters are summarized in Tab. 1. Forty-five sets of plasma parameters approximately evenly distributed in this parameter space are selected as input in simulations, as shown in numbered squares in Fig. 1. The three-dimensional PIC code PTetra (Marchand, 2012; Marchand & Lira, 2017) is used to simulate probe currents in this study. In the simulations, space is discretized using unstructured adaptive tetrahedral meshes (Frey & George, 2007; Geuzaine & Remacle, 2009). Poisson's equation is solved at each time step using Saad's GMRES sparse matrix solver (Saad, 2003) in order to calculate the electric field in the system. Then, electron and ion trajectories are calculated kinetically using their physical charges and masses self consistently. The mesh for the m-NLP and the simulation domain illustrated in Fig. 2, is generated with GMSH (Geuzaine & Remacle, 2009). The needle probe used in the simulation has a length of 25 mm and a diameter of 0.51 mm, as those on the NorSat-1. The needle probe is attached to a 15 mm long and 2.2 mm diameter guard which is biased to the same voltage as the probe. The outer boundary of the simulation domain is closer to the probe on the ram side, and farther on the wake side, as shown in Fig. 2. The simulations are made using two different domain sizes depending on the Debye length of the plasma. For plasma density below $2\times10^{10}$ m$^{-3}$ corresponding to a Debye length of 1.9-7.2 cm, a lager domain is used. For plasma density above $2\times10^{10}$ m$^{-3}$, corresponding to a Debye length of 0.2-2.2 cm, a smaller domain with finer resolution is used. The simulation size, the resolution, the number of tetrahedra, and the corresponding Debye length are summarized in Tab. 2. There is overlap between the two simulation domains for simulations with Debye lengths around 2 cm. However, no obvious difference was found in the simulated currents, indicating simulation results from both domains are consistent in the transition range. Simulation results from both domains are included when training the regression models. All simulations are run initially with 100 million ions and electrons, but these numbers vary through a simulation, due to particles being collected, leaving, or entering the domain. In the sim-

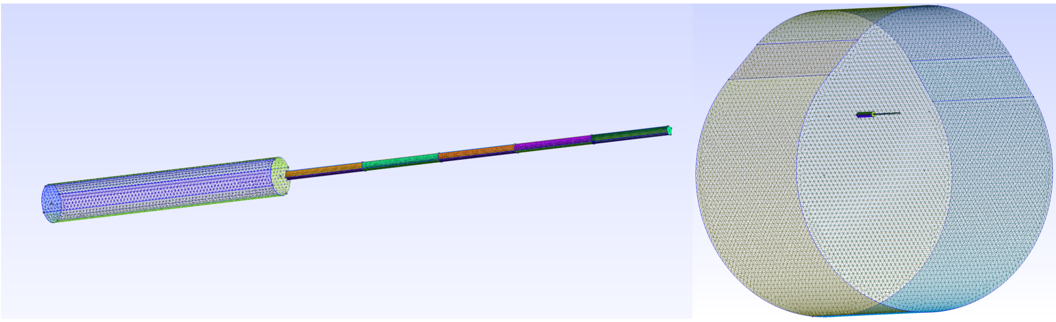

**Figure 2.** Illustration of a m-NLP geometry (left), and the simulation domain (right). The needle probe has a length of 25 mm, with a guard of 15 mm. The ram direction is from the top of the simulation domain.

**Table 1.** Spatial and temporal parameters used to sample ionospheric plasma conditions in IRI, and the corresponding ranges in space plasma parameters.

| Environment and plasma conditions | Parameter range |
|---|---|
| Years | 1998 2001 2004 2009 |
| Dates | Jan 4 Apr 4 Jul 4 Oct 4 |
| Hours | 0-24 with increment of 8 hours |
| Latitude | $-90°$ - $+90°$ with increment of 5° |
| Longitude | 0° - $-360°$ with increment of 30° |
| Altitude | 550-650 km with increment of 50 km |
| | |
| Ion temperature | 0.07-0.16 eV |
| Electron temperature | 0.09-0.25 eV |
| Effective ion mass | 2-16 amu |
| Density | $2 \times 10^9 - 1 \times 10^{12} \mathrm{m}^{-3}$ |

ulations, the probe is segmented into five segments of equal length, making it possible to estimate a rough distribution of the current along its length. The current used to build regression models is a sum of the currents of the five different segments. The orbital speed of the satellite is assumed to be fixed at 7500 m/s in the simulations, with a direction perpendicular to the probe. For the voltages considered, probes are expected to collect mainly electron currents. For simplicity, only two types of ions are considered in the simulation, $O^+$ and $H^+$ ions, and no magnetic field is accounted for in the simulation, which is justified by the fact that the Larmor radius of the electron considered is much larger than the radius of the probe.

### 2.2 Synthetic solution library

In order to assess the inference skill of a regression model, a cost function is defined with the following properties: i) it is positive definite, ii) it vanishes if model inferences agree exactly with given data in a data set, and iii) it increases as inferences deviate from actual data. The cost functions used in this work are: the root mean square

**Table 2.** Parameters used in the two simulation domains are listed. The first two columns listed the distances between the probe to the ram and the wake face of the outer boundary, followed by the simulation resolutions at the probe, guard, and the outer boundary. The number of tetrahedra used in the simulations is in the order of millions. The corresponding range in Debye lengths is also listed.

| Ram distance | Wake distance | Probe resolution | Guard resolution | Boundary resolution | Tetrahedra | Debye length |
|---|---|---|---|---|---|---|
| 3.5 cm | 7 cm | 51 $\mu$m | 220 $\mu$m | 2 mm | 2.5 M | 0.2-2.2 cm |
| 30 cm | 40 cm | 51 $\mu$m | 220 $\mu$m | 1 cm | 1.7 M | 1.9-7.2 cm |

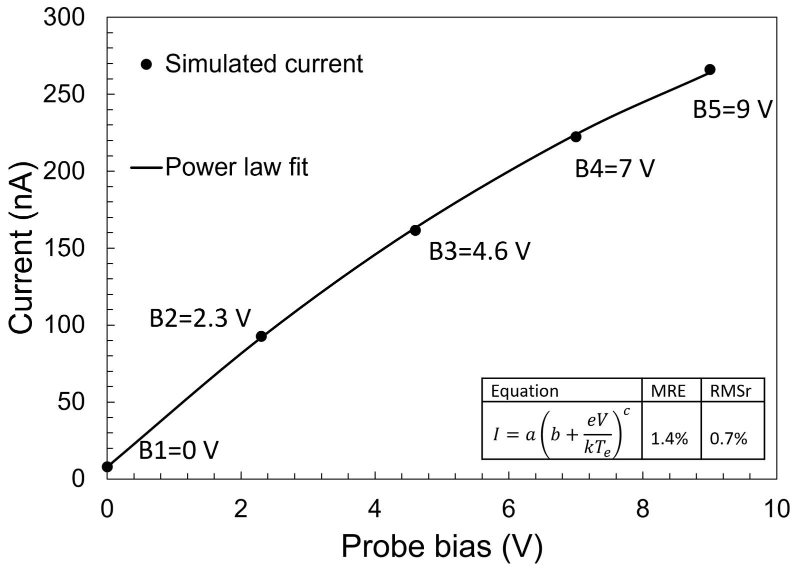


**Figure 3.** Example of simulated currents and fit for a set of plasma conditions. 5 probe voltages are simulated for each set of plasma conditions, and a power law fit is used to approximate the currents vs probe voltage characteristic. The fitting errors in the figure is calculated over all 45 sets of plasma conditions. The plasma conditions used in this graph are $2 \times 10^{10}$ m$^{-3}$, 8 amu, 0.15 and 0.12 eV for density, ion effective mass, electron temperature and ion temperature respectively.

error,

$$RMS = \sqrt{\frac{1}{N_{data}} \sum_{i=1}^{N_{data}} \left(Y_{mod_i} - Y_{data_i}\right)^2}, \tag{2}$$

the root mean square relative error

$$RMSr = \sqrt{\frac{1}{N_{data}} \sum_{i=1}^{N_{data}} \frac{\left(Y_{mod_i} - Y_{data_i}\right)^2}{Y_{mod_i}^2}}, \tag{3}$$

the maximum absolute error

$$MAE = \max\left\{|Y_{mod} - Y_{data}|\right\}, \tag{4}$$

and the maximum relative error

$$MRE = \max\left\{\left|\frac{Y_{mod} - Y_{data}}{Y_{mod}}\right|\right\}, \tag{5}$$

where $Y_{data}$ and $Y_{mod}$ represent respectively known and inferred plasma parameters, and $N_{data}$ is the total number of data points.

For each of the 45 sets of plasma parameters illustrated in Fig. 1, simulations are made assuming 5 probe voltages with respect to background plasma, and the simulated currents vs probe voltage are approximated using a power-law fit with three fitting parameters

$$I = a\left(b + \frac{eV}{kT_e}\right)^c. \tag{6}$$

The MRE calculated for all 45 fits is 1.4%, and the RMSr is 0.7%, which shows excellent agreement with simulated collected currents. A comparison between fitted and computed currents is shown in Fig. 3.

The NorSat-1 m-NLP probes are biased to +10, +9, +8, and +6 V with respect to the spacecraft, and the probe voltage with respect to background plasma is given by the sum of the spacecraft floating potential plus the probe bias $V = V_f + V_b$. In simulations, probe currents for voltages with respect to background plasma in the range between 0 to 9 volts are considered as shown in Fig. 3. Considering that the probe bias voltages $V_b$ are +10, +9, +8 and +6 V, for any given floating potential $V_f$ in the range of -1 to -6 V, the probe voltage $V$ with respect to the background plasma is in the range of 0 to 9 V covered in the simulations. A synthetic solution library is created by assuming randomly distributed spacecraft floating potentials in the range between -1 and -6 V and interpolating the corresponding currents at these voltages using Eq. 6 with the fitting parameters from the 45 fits as shown in Fig. 3. The synthetic solution library constructed from simulations, consists of four currents collected by the four needle probes at the four different bias voltages, for 160 randomly distributed spacecraft potentials in the range between -1 V to -6 V for each of the 45 sets of plasma parameters. In each entry of the data set, these four currents are followed by the electron density, the spacecraft potential the electron and ion temperatures, and the ion effective mass. The resulting solution library consisting of $45 \times 160 = 7200$ entries is then used to construct a training set with 3600 randomly selected nodes or entries, and a validation set with the remaining 3600 nodes. The cost functions reported in this paper are all calculated from the validation data set unless stated otherwise.

### 2.3 Multivariate regression

The next step is to make a multivariate regression model that maps the currents to the corresponding plasma conditions in the solution library. In a complex system where the relation between independent variables and dependent variables cannot readily be cast analytically, multivariate regressions based on machine learning techniques are powerful alternatives to construct approximate inference models. In this approach, the model must be capable to capture the complex relationship between dependent and independent variables. Once the model is trained using the training set, it can then be used to make inferences where the dependent variable is not known. In this work, two multivariate regression approaches are used to infer plasma parameters: the Radial Basis Function and Feedforward Neural Networks. The models are trained by optimizing their cost function on the training data set, and then applied to the validation data set to calculate the validation cost function without further optimization. The use of a validation set is to avoid "overfitting" because there are certain limitations on the refinement of a model on a training set, such that further improvement of model inference skill in the training set will worsen the model inference skill in the validation set. A good model is one with the right level of training so as to provide the best inference skill in the validation set.

#### 2.3.1 Radial basis function

Radial basis function (RBF) multivariate regression is a simple and robust tool used in many previous studies to infer space plasma parameters using a variety of instruments with promising results (Liu & Marchand, 2021; Olowookere & Marchand, 2021; Chalaturnyk & Marchand, 2019; Guthrie et al., 2021). A general expression for RBF regression for a set of independent n-tuples $\bar{X}$ and corresponding dependent variable $Y$ is given by:

$$Y = \sum_{i=1}^{N} a_i G\left(\left|\bar{X} - \bar{X}_i\right|\right). \tag{7}$$

In general, the dependent variable $Y$ can also be a tuple, but for simplicity, and without loss of generality, we limit our attention to scalar dependent variables. In Eq. 7, the $\bar{X}_i$ represents the $N$ centers, $G$ is the interpolating function, and the $a_i$ are collocation coefficients which can be determined by requiring collocation at the centers; that is, by solving the system of linear equations

$$\sum_{i=1}^{N} a_i G(|\bar{X}_k - \bar{X}_i|) = Y_k \tag{8}$$

for $k = 1,\ ...,\ N$. Here, the dependent variable $Y$ corresponds to the physical parameter to be inferred, the independent variable $\bar{X}$ is a 4-tuple corresponding to the currents or the normalized currents from the m-NLPs depending on which physical parameters are being inferred. There are different ways to distribute the centers in RBF regression, one straightforward approach is to evaluate the cost function over the entire training data set for all possible combinations of centers, then select the model which yields the optimal cost function. For this approach, the number of combinations required for $\mathcal{N}$ data points and $N$ centers is given by

$$\binom{\mathcal{N}}{N} = \frac{\mathcal{N}!}{N!(\mathcal{N} - N)!}. \tag{9}$$

This, of course, can be prohibitively large and time-consuming for a large training data set or using a large number of centers. An alternative strategy is to successively train models with randomly selected small subsets of the entire training data set using the straightforward approach, then carrying the optimal centers from one iteration to the next. This "center-evolving strategy" is very efficient in finding near-optimal centers for large training data sets and has proven to be as accurate as the straightforward extensive approach. The RBF models here follow this procedure. Different G functions and cost functions are tested, and only the models that yield optimal results are reported in this paper.

#### 2.3.2 Feedforward neural network

The second multivariate regression approach is a Feedforward neural network as illustrated in Fig. 4. This consists of an input layer, hidden layers, and an output layer.

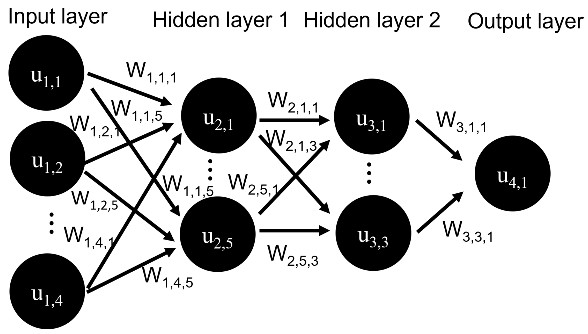


**Figure 4.** Schematic of a feedforward neural network.

Each node $j$ in a given layer $i$ in the network is assigned a value $u_{i,j}$, and the node in the next layer $i{+}1$ are "fed" from numerical values from the nodes in the previous layer according to

$$u_{i+1,k} = f\left(\sum_{j=1}^{n_i} w_{i,j,k} u_{i,j} + b_{i,k}\right), \tag{10}$$

where $w_{i,j,k}$ are weight factors, $b_{i,j}$ are bias terms, and $f$ is a nonlinear activation function (Goodfellow et al., 2016). In this work, the input layer neurons contain the four-needle probe currents or normalized needle probe currents depending on the physical parameter to be inferred, whereas the output layer contains one physical parameter. The number of hidden layers and the number of neurons in the hidden layers are adjusted to fit the specific problem, and attain good inference skills. The Feedforward neural network is built using TensorFlow (Abadi et al., 2016) with Adam optimizer (Kingma & Ba, 2015), and using the ReLU activation function defined as $f(x) = max(0, x)$. The input variables are normalized using the `preprocessing.normalization` function built-in in TensorFlow which normalizes the data to have a zero mean and unit variance. The structure of the network will be described later when presenting the model inferences.

## 3 Assessment with synthetic data

In this section, we assess our models using synthetic data, which allows us to check the accuracy, and quantify uncertainties in our inferences. A consistency check strategy is also introduced to further assess the applicability of our models.

### 3.1 Density inference

The density can be inferred using Eq. 1 which can be rewritten as:

$$\frac{n_e}{T_e^{\beta-\frac{1}{2}}} = \sqrt{\frac{\pi^2 m_e}{2A^2e^3}}\left(\frac{I_1^{\frac{1}{\beta}} - I_2^{\frac{1}{\beta}}}{V_1 - V_2}\right)^{\beta}. \tag{11}$$

In this equation, subscripts 1 and 2 indicate different probes. One requirement for using this equation is that $\beta$ be 0.5. In this case the equation take form of:

$$n_e = \sqrt{\frac{\pi^2 m_e}{2A^2e^3}}\sqrt{\frac{I_1^2 - I_2^2}{V_1 - V_2}}. \tag{12}$$

As a result, the power term on electron temperature vanishes, and the density can be determined independently of temperature. With currents from two probes, the density

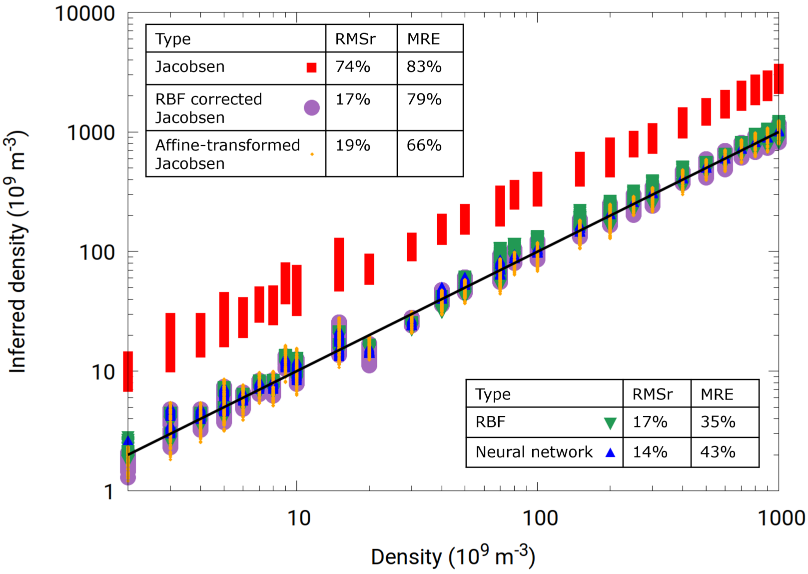


**Figure 5.** Correlation plot for the density inferences made with different techniques applied to our synthetic validation set.

can be calculated from the slope of the current squared over bias voltage from a least-square fit of all probes as first suggested by Jacobsen (Jacobsen et al., 2010). On the other hand, the $\beta = 0.5$ assumption requires that the needle probe be very long compared to the Debye length, which is in general not satisfied for NorSat-1 satellite. As a consequence, when this method is applied to the solution library, the inferred density is typically three times higher than the actual density as shown with red boxes in Fig 5. Despite the offset, this method produces densities which closely follow the true density in the synthetic data set. This offset can be reduced by dividing the calculated density by three, but better accuracy can be achieved using an affine transformation applied to the natural log of the inferred density:

$$\ln(n'_e) = a \ln(n_e) + b. \tag{13}$$

In this equation, the density $n_e$ is first obtained using the Jacobsen approach, then affine transformation is used to calculate the inferred density $n'_e$. The affine transformation coefficients a and b are obtained from a least-squares fit of the log of these densities, to those in the training data set. The fitting coefficients in this case, $a = 1.13$ and $b = -4.83$, are then used to perform an affine transformation on the validation data set leading to a significant improvement in RMSr from 74% to 19%, and in MRE from 83% to 66% compared to Jacobsen's densities, as shown in Fig 5. RBF regression can also be used to correct Jacobsen's density. This is done by using RBF to approximate the discrepancy between the true density and the one inferred with Jacobsen's technique. This correction is then used to improve the accuracy of the inferred density obtained with Jacobsen's method. Using the four currents as input variable $\bar{X}$, by minimizing the MRE, using $G(x) = x$, and 5 centers, the RBF corrected Jacobsen density yields a RMSr of 17 % and a MRE of 79%. The cost functions of the two methods are comparable, but an obvious advantage of using an affine transformation is its simplicity.

Direct RBF regression can be applied to infer density using the four currents as input variables. When constructing an RBF model with $G(x) = x$, minimizing MRE, and using 5 centers, the RMSr and MRE calculated on the validation data set are 17% and 35% respectively. Using a neural network with 4 nodes in the input layer, 14 nodes

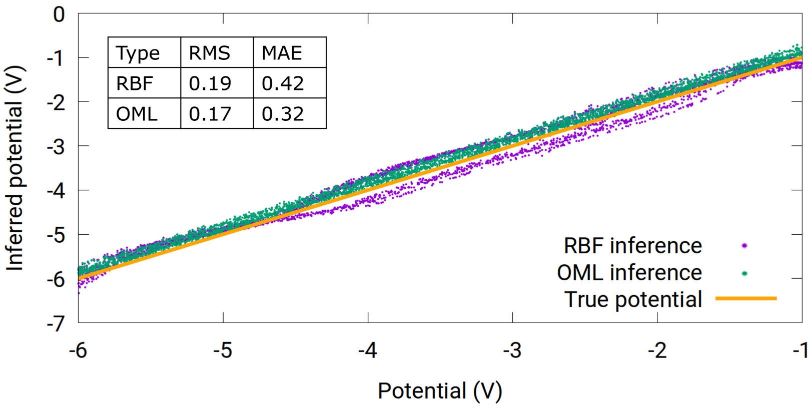


**Figure 6.** Correlation plot obtained for satellite potential inferred with RBF and OML techniques.

and 12 nodes in two hidden layers, and 1 node in the output layer, the calculated density achieves a 14% RMSr and 43% MRE. This is calculated using TensorFlow with ADAM optimizer with a learning rate of 0.005 and a RMSr as a cost function. The input layer is normalized to have a zero mean and unit variance, while the output layer is normalized by dividing the largest density. The densities calculated using synthetic solution library, as well as the cost function are shown in Fig. 5. Compared to the other density models considered, straightforward RBF yields the smallest MRE, thus it is the preferred model to infer density in this work. However, the affine-transformed Jacobsen technique enables inferences with accuracy comparable to those of more complex approaches. This simple and practical technique should be considered in routine data analysis.

### 3.2 Potential inference

The floating potential of the spacecraft can also be inferred using the OML equation, by rewriting equation 1 as:

$$V_f \approx V_f + \frac{kT_e}{e} = \frac{V_2 I_1^{\frac{1}{\beta}} - V_1 I_2^{\frac{1}{\beta}}}{I_2^{\frac{1}{\beta}} - I_1^{\frac{1}{\beta}}} = \frac{V_3 I_2^{\frac{1}{\beta}} - V_2 I_3^{\frac{1}{\beta}}}{I_3^{\frac{1}{\beta}} - I_2^{\frac{1}{\beta}}} \tag{14}$$

In this equation, the subscripts 1,2, and 3 refer to different probes, thus there must be at least three probes in order to solve for $\beta$. The bias voltage of the probes and their corresponding collected currents are known from measurements, thus $\beta$ can be solved using a standard root finder. Given $\beta$, equation 14 then provides a value for $V_f + \frac{kT_e}{e}$. In this expression, $\frac{kT_e}{e}$ is the electron temperature in electron-volt, which in the lower ionosphere, is of order 0.3 eV or less. Thus, considering that $\frac{kT_e}{e}$ is generally much smaller than satellite potentials relative to the background plasma, any of the two terms in the right side of Eq. 14 provide a first approximation of $V_f$. This equation works very well when it is applied to the synthetic solution library with a MAE of 0.3 V calculated using 10, 9, and 8 volts probes. The error of 0.3 V is likely due to the maximum electron temperature of 0.3 eV considered in the simulations. The $\beta$ calculated in the synthetic solution library is in the range of 0.75 to 1. It is also possible to build a model to infer floating potentials directly using RBF regression. In this case, currents are normalized by dividing every current by their sum, in order to remove the strong density dependence on the currents. Using $G(x) = x$, and 5 centers, and minimizing MAE, the calculated MAE on the validation data set is 0.4 V. A correlation plot for OML inference, and RBF inferences of potentials are shown in Fig. 6. Both methods show good agreement with values from the synthetic solution library.

### 3.3 Consistency check

In order to further assess the applicability of our inference approaches, we perform a consistency check consisting of the following. First, RBF models $M1(n_e)$ and $M1(V_f)$) are constructed to infer the density and satellite potential using 4-tuple currents from our synthetic data set. A second model ($M2$) is constructed to infer collected currents from densities and floating potentials in our synthetic data set. Since we are not able to infer temperatures from the currents, the temperature is not included in $M2$. Consistency is then assessed in two steps by i) using currents from synthetic data and models $M1(n_e)$ and $M1(V_f)$ to infer densities and floating potentials, and ii) applying models $M2$ to these inferred values to infer back collected currents. RBF density and floating potential inferences are used in $M1(n_e)$, and $M1(V_f)$ as described in sec. 3.1 and 3.2. RBF is also used in $M2$ with $G(x) = \sqrt{1 + x^{2.5}}$, and minimizing RMSr with 5 centers. With perfect inference models, the results for these back-inferred currents, should agree exactly with the starting currents from synthetic data. Variances between back-inferred and simulated currents in the synthetic data are presented as indicative of the level of confidence in our regression techniques. The correlation plot in Fig. 7, shows back-inferred currents calculated for a probe with 10 V bias against known currents from synthetic data. For comparison, the figure also shows the correlation between directly in-

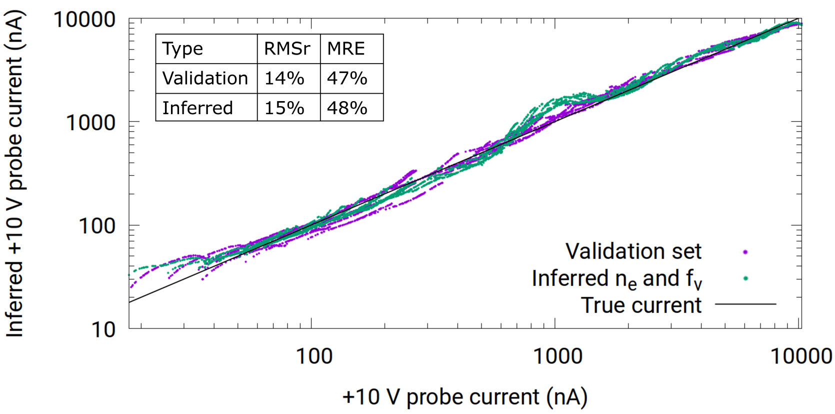


**Figure 7.** Correlation plot of inferred +10 V probe current against +10 V probe current from the synthetic data set is presented. The calculated +10 probe currents in purple curve is calculated using the validation data set, while the green curve is calculated using inferred densities and floating potentials from RBF regression.

ferred currents when model $M_2$ is applied to densities and floating potentials from the synthetic data set. Both back-inferred and directly inferred currents are in excellent agreement with known currents from synthetic data, with comparable metric skills of $\simeq 15\%$ and $\simeq 48\%$ for the RMSr and the MRE, respectively. Considering that errors are compounded between the first and second models for the back-inferred currents, the nearly identical metric skills seen in Fig. 7 is seen as confirmation of the validity of our regression models.

# 4 Application to NorSat-1 data

In this section, we apply our density and potential inference models constructed with synthetic data, to in situ measurements made with the m-NLP on the NorSat-1 satellite. The NorSat-1 currents were obtained from a University of Oslo data portal (Hoang, Clausen, et al., 2018). The epoch considered corresponds to one and a half orbit of the satellite starting at approximately 10:00 UTC on January 4, 2020. We start with a comparison of simulated and measured currents to verify that our simulated currents are in the same range as that of measured in situ currents. Densities inferred with RBF, neural network, and the two corrected Jacobsen's methods constructed in 3.1, are also presented.

## 4.1 Measured in-situ, and simulated currents

The instrumental limit for the NorSat-1 m-NLP probes is estimated to be approximately 1 nA (Hoang, Clausen, et al., 2018). However, in order to ensure a sufficient signal-to-noise ratio, a lower bound of 10 nA should be applied for all four probes, as the noise level of the environment is now estimated to be of order 10 nA. This is done by filtering out all data that contain a current that is below 10 nA in any of the four probes. The +9 V probe currents against the +10 V probe currents for both NorSat-1 data above 10 nA, and the corresponding currents from the synthetic data set are plotted in Fig. 8. The

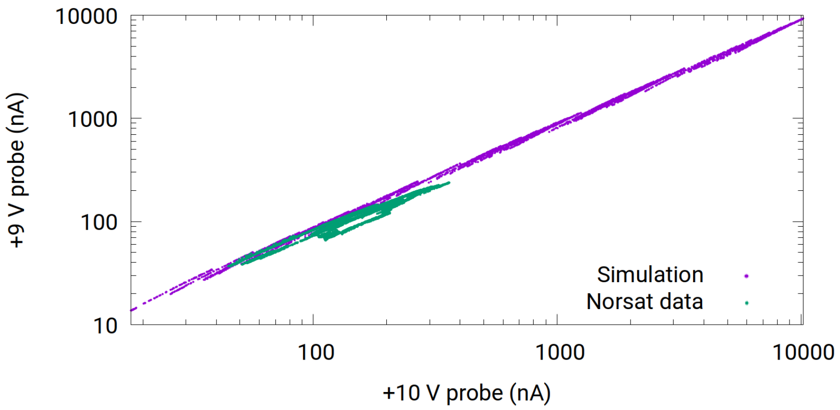


**Figure 8.** Correlation plot between currents collected by the +9 V and the +10 V probes for both NorSat-1, and synthetic data.

overlap between the two sets of currents, and the fact that simulated currents cover a wider range, indicates that our synthetic data should be applicable to NorSat measured currents.

## 4.2 Density and satellite potential inference

Our models, trained with synthetic data as described in Sec. 3, are now applied to infer plasma densities and satellite potentials from in situ measured currents, for the time period considered. The results obtained with the different models presented in Sec. 3 are shown in Fig. 9 for the inferred densities, satellite potentials, and measured currents collected by the four probes. The position of the satellite relative to the Earth and the Sun given by the solar zenith angle, is also plotted in the figure. For example, a small solar zenith angle means that the satellite is near the equator on the dayside. This figure also shows inferences for densities and floating potentials using data in which the low-

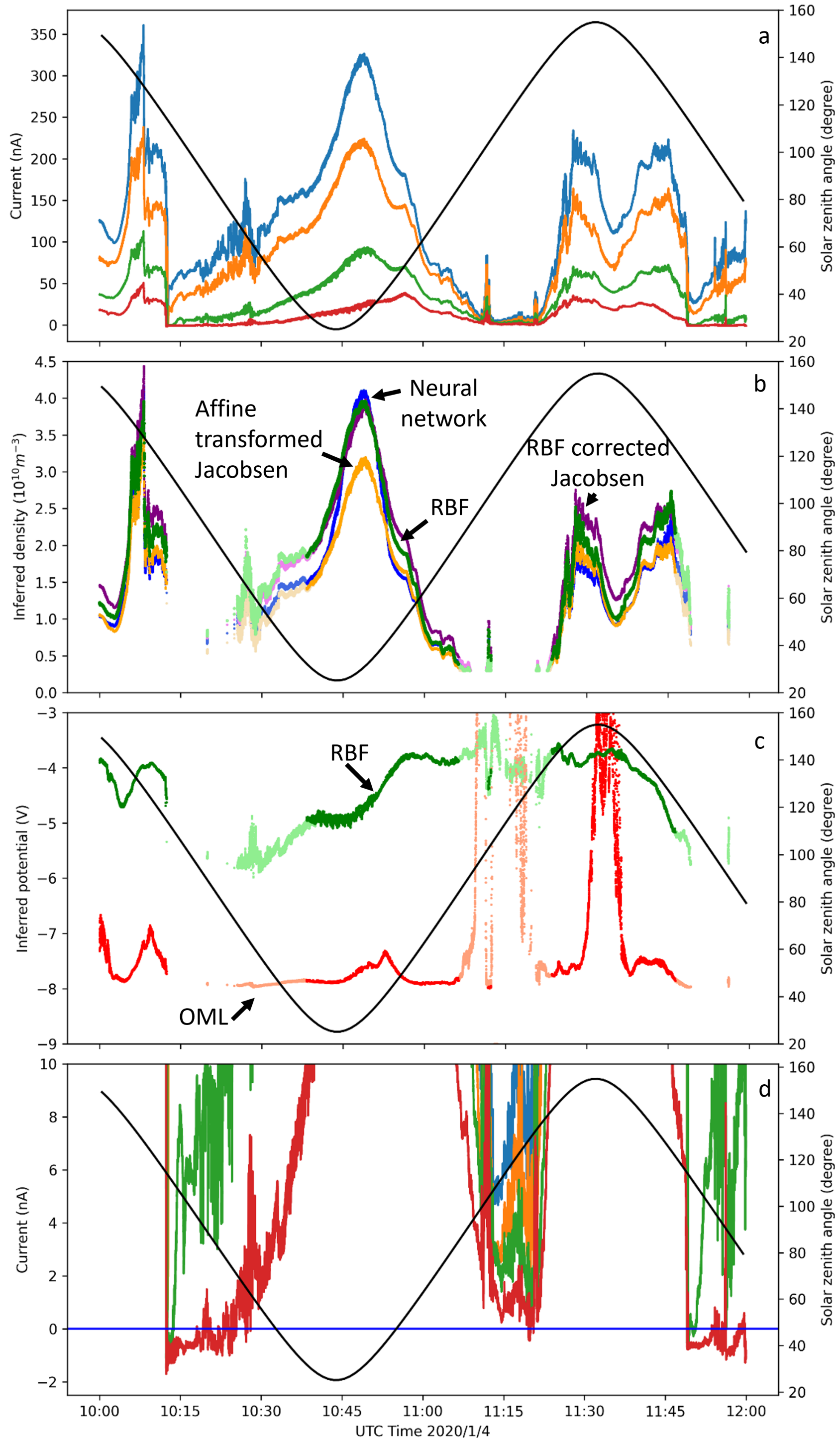


**Figure 9.** Illustrations of NorSat-1 collected currents considered in this study in panel a, inferred densities in panel b, inferred potentials in panel c, and the NorSat-1 current near 0 A in panel d. The solar zenith angle is also plotted against the secondary axis. Curves in darker colors are from model inferences using data above 10 nA, whereas those in lighter colors show inferences using data with currents between 1 nA and 10 nA.

est collected current is between 1 nA and 10 nA in lighter colors, to demonstrate that our model inferences made with these lower currents, remain consistent with those obtained with currents above 10 nA. A word of caution is in order, however, for inferences made from these lower currents, as a conservative estimate of the threshold for acceptable signal-to-noise ratios, is approximately 10 nA. This lower bound on acceptable currents is supported by a consistency check made with models 1 and 2 described in Sec. 3.3, and presented below in Sec. 4.3.

The densities shown in Fig. 9 panel b are obtained using the four density inference methods mentioned in Sec. 3.1. Direct Jacobsen's density is not shown as it is too large by about a factor of 3. At 10:45, neural network density, RBF corrected Jacobsen density, and RBF density overlap nicely, while affine transformed Jacobsen density inferences are smaller than other inferred densities, particularly near the density maxima. The density inferences at other ranges nevertheless agree with each other nicely. Using the preferred RBF inferred density as base and data above 10 nA, the calculated RMSr is 15% and the MRE is 29% using densities calculated from other techniques.

Using the +10, +9, and +8 NorSat-1 probe currents and Eq. 14 for the OML approximation, the inferred satellite floating potential is about -8 V for most of the data range considered in this study as shown in Fig. 9 panel c. This is in stark contradiction with observations in Fig. 9 panel d, which shows that the +6V biased probe collects net positive electrons during most of the period considered. However, there are periods between 10:15 to 10:30, and after 11:45 when the + 6V probe collects ion current(negative), indicating drops in the satellite potential below -6V. The poor performance of OML to infer the satellite potential here, results from the fact that Eq. 14 yields erratic values of $\beta$ ranging from 0.3 to 1.2. Attempts have also been made to approximate the satellite potential with Eq. 14 using a fixed value of 0.58 and 0.78 for $\beta$, also resulting in satellite potentials in the $-8$ V range, and no improvement was found. This failure to produce acceptable values of the satellite potential clearly show that this generalized OML approximation in Eq.14 is not applicable to NorSat-1 satellite data.

As a test, the RBF model trained with synthetic data set is applied to measured currents between 1 and 10 nA. The inferred densities and satellite potentials appear in Fig. 9 are in lighter colors. Interestingly, the inferred satellite potential is seen to join smoothly with the darker color inferences, and to decrease below -6 V around 10:25, where the current from the +6 V biased probe becomes negative, indicating that it collects mostly ions. In Fig. 9, the density and floating potential are seen to peak at around 10:45 and 11:00 respectively. The two major factors that influence the probe current collection are density and floating potential. The currents from the +8, +9, and +10 V probes (green, orange, and blue) in panel a peak at around 10:45, coinciding with the peak in the plasma density at this time. Then, as time goes forward to 11:00, the currents of the three probes decrease, also coinciding with a decrease in plasma density. However, the +6 V probe (red) current is increasing during these times, likely due to an increase in floating potential. This increase is captured in the RBF inferred floating potential but not in the one obtained from OML. Another observation is that the inferred floating potential decreases significantly at 10:15, as the satellite crosses the terminator. On NorSat-1, the negative terminals of the solar cells are grounded to the spacecraft bus while the positive side is facing the ambient plasma (Ivarsen et al., 2019). A likely explanation for the potential drop is that the solar cells facing the ambient plasma get charged positively and is suddenly starting to collect more electrons upon exiting solar eclipse. This would agree with findings reported by Ivarsen et al. (Ivarsen et al., 2019).

### 4.3 Consistency check

In the absence of accurate and validated inferred densities and satellite potentials from NorSat-1 data, it is not possible to confidently ascertain to what extent the infer-

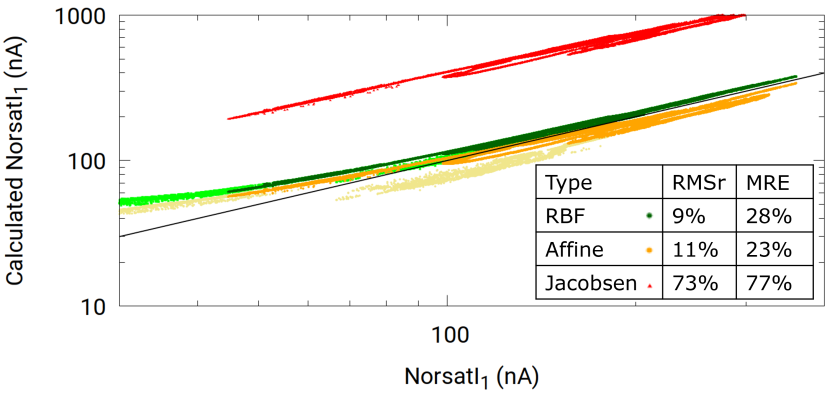


**Figure 10.** Consistency check is performed in the in situ data following the same procedure as in the synthetic data set. Both models 1 and 2 are trained with our synthetic data, and applied to currents from the +10 V probe on NorSat-1. Darker colors refer to inferences made with current above 10 nA, while lighter colors refer to inferences obtained with currents between 1 and 10 nA.

ences presented above are accurate. We therefore proceed with a consistency check, following the same procedure as presented in Sec. 3.3 for synthetic data, but using measured currents as input. This is done by first applying $M1(n_e)$ and $M1(V_f)$) trained with synthetic data, to infer floating potentials and densities from measured currents. Then $M2$ (also trained with synthetic data) is used to infer currents from the $M1$ - inferred floating potentials and densities. If the models constructed from the synthetic data also apply to NorSat-1 data, the inferred currents should closely reproduce the measured NorSat-1 currents. A correlation plot of inferred against measured currents is shown in Fig. 10 for the +10 V probe. In this plot, the green and orange curves are obtained from $M_2$ using densities inferred from currents obtained with direct RBF, and transformed Jacobsen in $M1(n_e)$, and direct RBF potentials in $M1(V_f)$. The parts in lighter color are obtained using data with a 1nA filter, whereas the darker color parts are obtained using data with currents above 10 nA. Inferred currents based on Jacobsen's density ($\beta$=0.5) as $M1(n_e)$ are also plotted here as a comparison. While not shown, the 1 nA filter curve extends to the left down to about 5 nA, however, these calculated +10 volt probe currents plateau in this range and are far from the measured currents. This behavior is likely due to the noise level of the environment which is about 10 nA, thus extra caution should be taken when using model inferences for data below 10 nA. The RMSr calculated for the 10 nA NorSat-1 current using direct RBF density as $M1(n_e)$ is 9%, and the MRE is 28 %, whereas these numbers for affine transformed Jacobsen densities are 11 % and 23 %, respectively. These numbers are smaller than the RMSr and MRE calculated in the synthetic data set, likely due to the fact that in situ data covers a smaller range in density. The inferred currents calculated from $M2$ using Jacobsen's densities and RBF potentials, are significantly and systematically larger than the input currents, indicating that Jacobsen's densities alone are again, not applicable in this case. The calculated +10 V probe current based on RBF regression and affine transformed Jacobsen method nicely follows with the true +10 volt probe current except for a small increase in the variance at lower currents, thus indicating that our model constructed with synthetic data set should be applicable to in situ data.

## 5 Conclusions

A new approach is presented to infer plasma and satellite parameters from Langmuir probe measurements. The method consists of creating solution libraries with kinetic simulations capable to calculate probe measurements encountered by satellites in low Earth orbit conditions, and with physical processes, which cannot be accounted for analytically. Simulation results are then used to construct solution libraries from which multivariate regression inference models are constructed. In addition to accounting for more physical processes than possible in theories such as OML, this approach has the advantage of producing inferences with quantifiable uncertainties. The proposed simulation-regression approach is applied to the Norwegian satellite NorSat-1 m-NLP instrument as a case study. Four density inference techniques are used and compared for their inference skills, when applied to synthetic data, and actual measurements made in space. It is found, as reported in previous studies, that OML based inferences overestimate the plasma density by approximately a factor of three, when applied to our synthetic solution library. RBF regression is used to correct OML based inferences, the combined RBF-OML based inference, direct RBF inference, and the use of affine transformation applied to OML based inferences are found to yield excellent results. Another method considered is based on neural network regression. After applying and assessing all four models with our synthetic solution library, they are applied to the NorSat-1 m-NLP data. The density inference from all four methods shows good agreement, which we believe, is a significant improvement over the commonly used OML based inference method. Based on our findings, the direct RBF method and the affine transformed Jacobsen's method are the preferred methods to infer density. The direct RBF method yields the lowest maximum relative error, whereas the affine transformed Jacobsen's method is the simplest method and produces inferences with comparable accuracy. The spacecraft floating potential is also inferred using RBF regression and the OML approach. OML inferences are inconsistent with the measurements from NorSat-1 data since it indicates that the satellite potential is below -6V, while measurements indicate that the +6 V probe is collecting electron current. Conversely, spacecraft potentials inferred with RBF regression yield positive voltages for the probe when they collect electrons, which is more consistent with observation.

In the absence of validated and accurate measurements of density and spacecraft potential for Norsat-1 satellite, it is unfortunately impossible to ascertain to what extent our inference techniques improve inference skills compared to conventional techniques, largely based on analytic approximations. Therefore, in lieu of comparisons with accurate densities and satellite potentials, a consistency check is performed to assess the applicability and confidence level of our inference models. Compared to generally used analytic inference approaches, our simulation-regression based techniques will, of course, take more time to run and be trained. Our approach, however, has the advantage of accounting for more realistic conditions of geometry, and more physical processes than possible analytically, while being able of reproducing known analytic results under conditions where the assumptions made in these underlying theories are satisfied. The work presented here is by no means final. The development of improved inference approaches based on simulations and regression techniques will require significantly more efforts, involving collaborations between experimentalists and modelers; an effort well worth, considering the cost and years of preparation involved in scientific space missions.

**Acknowledgments**

This work was supported by the China Scholarship Council, the Natural Sciences and Engineering Research Council of Canada, the Research Council of Norway (Grant Agreement No. 275655 and 325074), and the European Research Council (ERC) under the European Union's Horizon 2020 research and innovation program (Grant Agreement No. 866357, POLAR-4DSpace). The kinetic simulations used in this study were made on the Compute Canada computing infrastructure. S.M. also acknowledges Dag Mortensen, Øyvind

Jensen, and the Institute for Energy Technology for permission to participate in this research.

## References


Abadi, M., Barham, P., Chen, J., Chen, Z., Davis, A., Dean, J., … others (2016). Tensorflow: A system for large-scale machine learning. In (p. 265-283).

Allen, J. E., Boyd, R. L. F., & Reynolds, P. (1957, 3). The collection of positive ions by a probe immersed in a plasma. *Proceedings of the Physical Society. Section B*, *70*, 297-304. Retrieved from `https://doi.org/10.1088/0370-1301/70/3/303https://iopscience.iop.org/article/10.1088/0370-1301/70/3/303` doi: 10.1088/0370-1301/70/3/303

Barjatya, A., & Merritt, W. (2018). Error analysis of multi-needle langmuir probe measurement technique. *Review of Scientific Instruments*, *89*, 1-5. Retrieved from `http://dx.doi.org/10.1063/1.5022820` doi: 10.1063/1.5022820

Bekkeng, T. A., Jacobsen, K. S., Bekkeng, J. K., Pedersen, A., Lindem, T., Lebreton, J. P., & Moen, J. I. (2010, 8). Design of a multi-needle langmuir probe system. *Measurement Science and Technology*, *21*, 085903. Retrieved from `https://iopscience.iop.org/article/10.1088/0957-0233/21/8/085903` doi: 10.1088/0957-0233/21/8/085903

Bernstein, I. B., & Rabinowitz, I. N. (1959). Theory of electrostatic probes in a low-density plasma. *Physics of Fluids*, *2*, 112. Retrieved from `https://aip.scitation.org/doi/10.1063/1.1705900` doi: 10.1063/1.1705900

Bhattarai, S., & Mishra, L. N. (2017, 8). Theoretical study of spherical langmuir probe in maxwellian plasma. *International Journal of Physics*, *5*, 73-81. Retrieved from `http://pubs.sciepub.com/ijp/5/3/2/index.html` doi: 10.12691/ijp-5-3-2

Bilitza, D., Altadill, D., Zhang, Y., Mertens, C., Truhlik, V., Richards, P., … Reinisch, B. (2014, 2). The international reference ionosphere 2012 – a model of international collaboration. *Journal of Space Weather and Space Climate*, *4*, A07. Retrieved from `http://www.swsc-journal.org/10.1051/swsc/2014004` doi: 10.1051/swsc/2014004

Chalaturnyk, J., & Marchand, R. (2019, 5). Regression-based interpretation of langmuir probe measurements. *Frontiers in Physics*, *7*. Retrieved from `https://www.frontiersin.org/article/10.3389/fphy.2019.00063/full` doi: 10.3389/fphy.2019.00063

Chen, F. F. (1965, 1). Numerical computations for ion probe characteristics in a collisionless plasma. *Journal of Nuclear Energy. Part C, Plasma Physics, Accelerators, Thermonuclear Research*, *7*, 47-67. Retrieved from `https://doi.org/10.1088/0368-3281/7/1/306https://iopscience.iop.org/article/10.1088/0368-3281/7/1/306` doi: 10.1088/0368-3281/7/1/306

Chen, F. F. (2003). Lecture notes on langmuir probe diagnostics. Mini-Course on Plasma Diagnostics, IEEEICOPS meeting. Retrieved from `http://www.seas.ucla.edu/~ffchen/Publs/Chen210R.pdf`

Frey, P., & George, P. L. (2007). *Mesh generation: Application to finite elements.* ISTE.

Geuzaine, C., & Remacle, J.-F. (2009, 9). Gmsh: A 3-d finite element mesh generator with built-in pre- and post-processing facilities. *International Journal for Numerical Methods in Engineering*, *79*, 1309-1331. Retrieved from `http://doi.wiley.com/10.1002/nme.2579` doi: 10.1002/nme.2579

Goodfellow, I., Bengio, Y., & Courville, A. (2016). *Deep learning.* MIT Press. Retrieved from `https://books.google.ca/books?id=Np9SDQAAQBAJ`

Guthrie, J., Marchand, R., & Marholm, S. (2021). Inference of plasma parameters from fixed-bias multi-needle langmuir probes (m-nlp). *Measurement Science and Technology*, *32*. doi: 10.1088/1361-6501/abf804

Hoang, H., Clausen, L. B., Røed, K., Bekkeng, T. A., Trondsen, E., Lybekk, B., … Moen, J. I. (2018, 6). The multi-needle langmuir probe system on board norsat-1. *Space Science Reviews*, *214*, 75. Retrieved from http://dx.doi.org/10.1007/s11214-018-0509-2http://link.springer.com/10.1007/s11214-018-0509-2 doi: 10.1007/s11214-018-0509-2

Hoang, H., Røed, K., Bekkeng, T. A., Moen, J. I., Clausen, L. B., Trondsen, E., … Sagi, E. (2019). The multi-needle langmuir probe instrument for qb50 mission: Case studies of ex-alta 1 and hoopoe satellites. *Space Science Reviews*, *215*. Retrieved from http://dx.doi.org/10.1007/s11214-019-0586-x doi: 10.1007/s11214-019-0586-x

Hoang, H., Røed, K., Bekkeng, T. A., Moen, J. I., Spicher, A., Clausen, L. B. N., … Pedersen, A. (2018, 6). A study of data analysis techniques for the multi-needle langmuir probe. *Measurement Science and Technology*, *29*, 065906. Retrieved from https://iopscience.iop.org/article/10.1088/1361-6501/aab948 doi: 10.1088/1361-6501/aab948

Hoskinson, A. R., & Hershkowitz, N. (2006). Effect of finite length on the current-voltage characteristic of a cylindrical langmuir probe in a multidipole plasma chamber. *Plasma Sources Science and Technology*, *15*, 85-90. doi: 10.1088/0963-0252/15/1/013

Ivarsen, M. F., Hoang, H., Yang, L., Clausen, L. B., Spicher, A., Jin, Y., … Lybekk, B. (2019). Multineedle langmuir probe operation and acute probe current susceptibility to spacecraft potential. *IEEE Transactions on Plasma Science*, *47*, 3816-3823. doi: 10.1109/TPS.2019.2906377

Jacobsen, K. S., Pedersen, A., Moen, J. I., & Bekkeng, T. A. (2010). A new langmuir probe concept for rapid sampling of space plasma electron density. *Measurement Science and Technology*, *21*. doi: 10.1088/0957-0233/21/8/085902

Johnson, J. D., & Holmes, A. J. T. (1990, 10). Edge effect correction for small planar langmuir probes. *Review of Scientific Instruments*, *61*, 2628-2631. doi: 10.1063/1.1141849

Kingma, D. P., & Ba, J. (2015). Adam: A method for stochastic optimization. In Y. Bengio & Y. LeCun (Eds.), . Retrieved from http://arxiv.org/abs/1412.6980

Laframboise, J. G. (1966). Theory of spherical and cylindrical langmuir probes in a collisionless, maxwellian plasma at rest. *Toronto Univ. (Ontario). Inst. for Aerospace Studies*. Retrieved from https://www.osti.gov/biblio/4522330

Lebreton, J.-P., Stverak, S., Travnicek, P., Maksimovic, M., Klinge, D., Merikallio, S., … Salaquarda, M. (2006, 4). The isl langmuir probe experiment processing onboard demeter: Scientific objectives, description and first results. *Planetary and Space Science*, *54*, 472-486. Retrieved from https://linkinghub.elsevier.com/retrieve/pii/S0032063305002084 doi: 10.1016/j.pss.2005.10.017

Lira, P. A. R., Marchand, R., Burchill, J., & Forster, M. (2019). Determination of swarm front plate's effective cross section from kinetic simulations. *IEEE Transactions on Plasma Science*, *47*, 3667-3672. doi: 10.1109/TPS.2019.2915216

Liu, G., & Marchand, R. (2021). Kinetic simulation of segmented plasma flow meter response in the ionospheric plasma. *Journal of Geophysical Research: Space Physics*, *126*. doi: 10.1029/2021JA029120

Marchand, R. (2012, 2). Ptetra, a tool to simulate low orbit satellite–plasma interaction. *IEEE Transactions on Plasma Science*, *40*, 217-229. Retrieved from http://ieeexplore.ieee.org/document/6069605/ doi: 10.1109/TPS.2011.2172638

Marchand, R., & Lira, P. A. R. (2017, 4). Kinetic simulation of spacecraft–environment interaction. *IEEE Transactions on Plasma Science*, *45*, 535-554. Retrieved from http://ieeexplore.ieee.org/document/7888602/

doi: 10.1109/TPS.2017.2682229

Marholm, S., & Marchand, R. (2020, 4). Finite-length effects on cylindrical langmuir probes. *Physical Review Research*, *2*, 023016. Retrieved from `https://link.aps.org/doi/10.1103/PhysRevResearch.2.023016` doi: 10.1103/physrevresearch.2.023016

Marholm, S., Marchand, R., Darian, D., Miloch, W. J., & Mortensen, M. (2019, 8). Impact of miniaturized fixed-bias multineedle langmuir probes on cubesats. *IEEE Transactions on Plasma Science*, *47*, 3658-3666. Retrieved from `https://ieeexplore.ieee.org/document/8734022/` doi: 10.1109/TPS.2019.2915810

Mott-Smith, H. M., & Langmuir, I. (1926). The theory of collectors in gaseous discharges. *Physical Review*, *28*, 727-763. doi: 10.1103/PhysRev.28.727

Olowookere, A., & Marchand, R. (2021). Fixed bias probe measurement of a satellite floating potential. *IEEE Transactions on Plasma Science*, *49*, 862-870. doi: 10.1109/TPS.2020.3045366

Rudakov, D. L., Boedo, J. A., Moyer, R. A., Lehmer, R. D., Gunner, G., & Watkins, J. G. (2001). Fast electron temperature diagnostic based on langmuir probe current harmonic detection on diii-d. *Review of Scientific Instruments*, *72*, 453-456. doi: 10.1063/1.1310577

Saad, Y. (2003). *Iterative methods for sparse linear systems* (Second ed.). Society for Industrial and Applied Mathematics. Retrieved from `https://epubs.siam.org/doi/abs/10.1137/1.9780898718003http://epubs.siam.org/doi/book/10.1137/1.9780898718003` doi: 10.1137/1.9780898718003

Sheridan, T. E. (2010, 3). The plasma sheath around large discs and ion collection by planar langmuir probes. *Journal of Physics D: Applied Physics*, *43*, 105204. doi: 10.1088/0022-3727/43/10/105204

Sudit, I. D., & Woods, R. C. (1994). A study of the accuracy of various langmuir probe theories. *Journal of Applied Physics*, *76*, 4488-4498. doi: 10.1063/1.357280